Effect of the deformation radius on the evolution of vortex properties in geostrophic turbulence

Jürgen Theiss*

Scripps Institution of Oceanography, University of California at San Diego, 9500 Gilman Dr., La Jolla, California 92093-0230, USA

(Received 18 December 2004; revised manuscript received 21 April 2005; published 21 September 2005)

Coherent vortices in geostrophic turbulence grow in size and become fewer as they merge. It is shown that the deformation radius L_D has no effect on the growth of the average vortex radius a as a grows from $a \ll L_D$ to $a \gg L_D$. Its growth is algebraic, given by $a \propto t^{\xi/4}$, where $\xi=0.72$. However, the deformation radius does have an effect on the decay of the number of vortices or vortex density ρ, given by $\rho \propto t^{-\xi}$ for $a \ll L_D$ and $\rho \propto t^{-\xi/2}$ for $a \gg L_D$. Thus the decay of ρ becomes slower once a has grown to a size comparable to that of L_D. One scaling theory for the entire range from $a \ll L_D$ to $a \gg L_D$ is presented and verified by numerical experiments. A special method for quadruplicating the numerical domain when the vortices become too few is proposed, which keeps the computation inexpensive. This work generalizes and agrees with previous work, in which the two special cases $a \ll L_D$ and $a \gg L_D$ are independently investigated.

DOI: 10.1103/PhysRevE.72.036304 PACS number(s): 47.27.Eq, 47.32.Cc

I. INTRODUCTION

Coherent vortices dominate the dynamics described by the simple quasi-two-dimensional model considered here. During the evolution of the dynamics, these vortices continuously merge and thus they grow in size and become fewer. We derive the laws given in the abstract, which quantitatively describe this growth and decay, respectively, and use numerical experiments to verify our assumptions, test our theoretical predictions, and determine parameters left undetermined by our derivation. The two opposite limits of our laws become identical to those of the two special cases considered previously [1,2], once an inconsistency with [2] is resolved.

The model is given by

$$\frac{\partial q}{\partial t} + J(\psi, q) = 0, \tag{1a}$$

where

$$q = \nabla^2 \psi - L_D^{-2} \psi \tag{1b}$$

is the potential vorticity. Time is denoted by t, $\nabla = (\partial/\partial x, \partial/\partial y)$, where x and y are horizontal coordinates, and $J(\psi, q) = \partial\psi/\partial x \partial q/\partial y - \partial q/\partial x \partial\psi/\partial y$, which is the Jacobian. The velocity is determined by $\mathbf{u} = \hat{\mathbf{k}} \times \nabla\psi$, where $\hat{\mathbf{k}}$ is the vertical unit vector. Depending on the application one has in mind, ψ and L_D are defined differently. In studies of plasmas, the equation above is known as the Charney-Hasegawa-Mima (CHM) equation [3,4]. It describes the dynamics of the electrostatic field on the plane perpendicular to a strong magnetic field uniformly applied to a plasma. In this case, ψ is the electrostatic potential and L_D the Larmor radius defined by $L_D = v_\perp / f_c$, where $v_\perp$ is the speed of a charged particle perpendicular to the magnetic field and f_c is the cyclotron frequency. In studies of the atmosphere and ocean, the equation is known as the quasi-geostrophic (QG) equation. It describes the slow, large-scale dynamics of a shallow layer of fluid with constant density ρ_1 above a deep layer with constant density $\rho_2 > \rho_1$ that is always at rest. This two-layer fluid is considered on a flat plane centered at a particular latitude θ_0 and thus the dynamics is described with respect to the rapidly rotating earth. In this case, ψ is the streamfunction and L_D the deformation radius defined by $L_D = \sqrt{g'H}/f_0$, where $\sqrt{g'H}$ is the shallow water gravity wave speed and f_0 is the value of the Coriolis frequency or parameter $f = 2\Omega \sin\theta$ at latitude $\theta = \theta_0$, where $\Omega = 2\pi/\text{day}$, which is the Earth's rotation rate. The presence of the lower layer has the effect of reducing the gravitational acceleration in the upper layer to $g' = (\rho_2 - \rho_1)/\rho_2 g$, where $g = 9.81\ \text{m/s}^2$ ([5] Sec. 2.12). If at rest, the upper layer has depth H. If the dynamics is strongly nonlinear it is referred to as geostrophic turbulence. The derivation of the equation and reasons that it is a useful approximation for studying the slow, large-scale dynamics of the atmosphere and ocean are given in many textbooks (e.g., [6] Sec. 12.2, [7] Sec. 3.12, [5] Sec. 2.6, noting that we consider here an f plane, that is, the approximation $f = f_0$). It is important to emphasize that the deformation radius is in this paper a constant, except in the last section in which we present an application of our results to a system with a latitude-dependent deformation radius. Throughout the paper, we use nomenclature and notations conventional in studies of the atmosphere and ocean. It must, however, be emphasized that our work is also applicable to studies of plasmas.

The finite size of the deformation radius L_D in (1b) makes geostrophic turbulence a useful generalization of intensely studied two-dimensional turbulence (e.g., [5] Sec. 4.8, [8]), given by the special case $L_D \to \infty$ in (1b). The general case can be considered to describe the dynamics of the upper layer of the ocean above an infinitely deep abyssal ocean that is at rest. It thus models the dynamics of a so-called first baroclinic mode. The interface between the two layers represents the ocean's thermocline. Physically, the deformation radius is a measure of the importance of thermocline fluctuations on the dynamics. For length scales smaller than the deformation radius, the extreme case being two-dimensional

*Email address: jtheiss@ucsd.edu

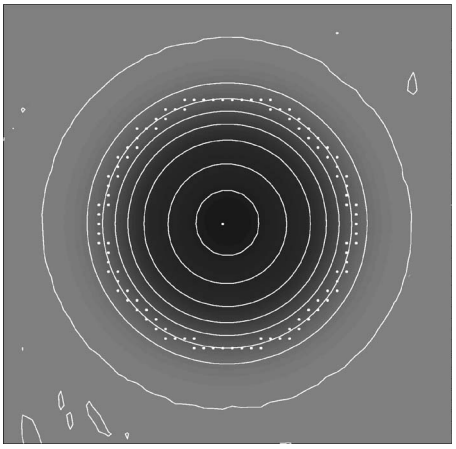

FIG. 1. McWilliams vortex census. This is an enlargement of the dotted box in Fig. 2(a), showing a coherent vortex in the potential vorticity field q. The contour lines represent the values of q from −70 to 0 with interval 10. The McWilliams vortex census determined the location of the vortex's extremum $q_{ext}=-77$ indicated by the dot in the middle and the vortex's boundary indicated by a circle of dots around the contour of $q=0.2q_{ext}$.

turbulence, the thermocline appears rigid and the two layers are practically uncoupled. For length scales larger than the deformation radius, the thermocline fluctuations dominate the dynamics. In this sense, a finite deformation radius captures the effect of the lower layer on the dynamics of the upper layer and thus incorporates the dynamical role of the vertical dimension in the quasi-two-dimensional geostrophic turbulence, which therefore represents a useful generalization of two-dimensional turbulence.

The geostrophic turbulence that we consider is the free evolution of a random initial state in a double periodic square domain of length L. The random initial state is here meant to be given in terms of an initial stream function whose Fourier components have phases that are random and amplitudes that give the energy spectrum $E(|\mathbf{k}|)$ in (12), which is given in terms of the total wave number $|\mathbf{k}|$ and has a sharp peak at high total wave number. In this geostrophic turbulence, coherent vortices of comparable radii and potential vorticity extrema emerge. To extend our study from such homogeneous to an inhomogeneous field of vortices, for instance one with a broad range of vortex radii, would be beyond the scope of this paper. For studies of such vortex dynamics see [8]. The average vortex radius a is determined by the McWilliams vortex census (Fig. 1) [9], which is an elaborate numerical scheme to detect coherent vortices and to determine their characteristics. In principle, it identifies extrema in the potential vorticity field q at a given time. It then searches for a closed boundary around every extremum, which is given by a closed contour line representing q values that are 80% smaller than the value of the extremum. In those cases in which an enclosed boundary exists, the area, say A, is only determined if the boundary has also a fairly circular shape. The radius is then given by $\sqrt{A/\pi}$. This allows to determine the average vortex radius a of the field of vortices at a given time. It is worth noting that not the particular contour line that leads to the size of a is significant, since the above 80% is somewhat arbitrary, but the particular form of the growth law. Apart from the average vortex radius a, we also determine the vortex density ρ at a given time, which is simply defined to be the number of vortices in the domain.

The remarkable property of (1) is that it conserves energy and enstrophy densities, denoted by $\mathcal{E}$ and $\mathcal{Z}$, respectively. This is shown by multiplying (1a) by ψ/L^2 and q/L^2, respectively, integrating over the domain, and using integration by parts. The energy density $\mathcal{E}$ thus takes the form

$$\mathcal{E}=\frac{1}{L^2}\int_{L^2}\frac{1}{2}[(\nabla\psi)^2+L_D^{-2}\psi^2]d\mathbf{x}, \tag{2}$$

where the first and second terms are the kinetic and potential energy densities, denoted by $\mathcal{E}_{kin}$ and $\mathcal{E}_{pot}$, respectively. If we then replace ψ by its Fourier integral, we have

$$\mathcal{E}=\int_0^\infty E(|\mathbf{k}|)d|\mathbf{k}|, \tag{3a}$$

$$\mathcal{Z}=\int_0^\infty (|\mathbf{k}|^2+L_D^{-2})E(|\mathbf{k}|)d|\mathbf{k}|. \tag{3b}$$

As the energy spectrum $E(|\mathbf{k}|)$ with the initial sharp peak, introduced above, spreads in wave number space, $\mathcal{E}$ and $\mathcal{Z}$ must be conserved. According to (3), this is only possible if more energy spreads to smaller rather than to larger $|\mathbf{k}|$. Energy is therefore said to cascade to larger length scales (e.g., [5] Sec. 4.8 for the special case of two-dimensional turbulence). The growing average vortex radius a considered here is a manifestation of this cascade.

Observations show that in the oceans most of the energy that is not in the mean flow is in length scales that are comparable to the deformation radius L_D (of the first baroclinic mode) [10]. However, the previously studied special cases mentioned in the abstract consider the energy to be in length scales that are either much smaller [1] or much larger [2] than L_D. These special cases, specified by $a\ll L_D\to\infty$ (two-dimensional turbulence) [1] and $a\gg L_D\neq 0$ [2], represent the two opposite limits of our model. Regarding the latter case, it is worth noting that the obvious limit $L_D\to 0$ cannot be considered because it would reduce (1a) to $\partial\psi/\partial t=0$. In this paper, we consider the general case for which a grows through a large range of values from $a\ll L_D$ to $a\gg L_D$. The benefit is an understanding on how L_D affects the evolution of vortex properties as the initially small a grows to the size of L_D and beyond. Since our general case also contains the case $a\approx L_D$, it captures therefore the dynamics relevant to studies of the ocean and also provides a more general view of vortex dynamics by achieving agreement with the two previously and independently studied special cases [1,2].

In order to numerically simulate the evolution of geostrophic turbulence through the necessary large range of values of the average vortex radius a, the resolution has to be sufficiently high to resolve the initially small scales and the domain size has to be sufficiently large to contain the final large vortices. Such a numerical simulation is computationally very costly. We therefore propose a technique, referred

to as quadruplication, that stepwise decreases an initially high resolution and increases an initially small domain size as the geostrophic turbulence freely evolves.

In Sec. II, we review the scaling theories developed for the two above-mentioned special cases [1,2] and propose a scaling theory for the general case. Section III explains the numerics, in particular the technique of quadruplication, and shows the results of the numerical experiments. A comparison and in particular a resolution of a disagreement with previous work is presented in Sec. IV. The insight developed in this paper is summarized in Sec. V and its application to a study of an equatorward energy cascade [11] is briefly explained in Sec. VI.

II. SCALING THEORY

A cascade of energy to larger length scales, which is in our model manifested by a growing average vortex radius a, is predicted using the conservation of energy density $\mathcal{E}$ and enstrophy density $\mathcal{Z}$ (see previous section). However, laws, as those in this section that quantitatively describe the evolution of vortex properties such as the growth of the average vortex radius a, can only be derived using, besides the conservation of energy density $\mathcal{E}$, also the conservation of potential vorticity extremum q_{ext}. Note that the former is a global conservation law whereas the latter is in a sense a local conservation law specific to the individual vortices.

To understand the conservation of potential vorticity extremum q_{ext}, we rewrite (1a) as $\partial q/\partial t+\mathbf{u}\cdot\boldsymbol{\nabla} q=0$, which shows that potential vorticity q in (1b) is conserved on fluid particles. This implies in particular that the vortex resulting from the merger of two vortices must have the larger potential vorticity extremum of the two potential vorticity extrema of the original two vortices [12]. If we assume for simplicity that all the potential vorticity extrema of an initial state have the same value q_{ext} then the potential vorticity extrema of all the vortices that exist during the evolution of the geostrophic turbulence must also all have that same value q_{ext}. Thus, q_{ext} is conserved. This has been numerically verified for the special case $a \ll L_D \to \infty$ (two-dimensional turbulence) ([9], his Fig. 7 and [1], their Fig. 1). For the opposite special case $a \gg L_D$ [2], it has not been shown previously, but our recreation of the numerical experiment of [2] provides the verification (not shown). For the general case, for which a ranges from $a \ll L_D$ to $a \gg L_D$, the numerical verification is presented in the next section and shown in Fig. 3(a). For the following we define $q_{ext}=q_{ext,kin}+q_{ext,pot}$ analogous to $\mathcal{E}=\mathcal{E}_{kin}+\mathcal{E}_{pot}$ in (2).

The scaling theory of the special case $a \ll L_D \to \infty$ (two-dimensional turbulence) [1] uses the conservation laws introduced above, which state in this special case that $\mathcal{E}_{kin}$ and $q_{ext,kin}$ are both constant. The expression for $\mathcal{E}_{kin}$ in (2) can be rewritten using integration by parts, which replaces $(\nabla\psi)^2$ by $\psi\nabla^2\psi$, and inserting $\psi(\mathbf{x})=\int G(\mathbf{x},\mathbf{x}')\nabla'^2\psi(\mathbf{x}')d\mathbf{x}'$, where $G(\mathbf{x},\mathbf{x}')$ is the Green function for ∇^2, leading to

$$\mathcal{E}_{kin}=\frac{1}{L^2}\int_{L^2}\int_{L^2}\frac{1}{2}q_{kin}(\mathbf{x})G(\mathbf{x},\mathbf{x}')q_{kin}(\mathbf{x}')d\mathbf{x}\,d\mathbf{x}', \qquad (4)$$

where $q_{kin}=\nabla^2\psi$. Assuming that most potential vorticity is contained in vortices and that those contributions to the integrals in (4) are negligible that arise when two locations, represented by the values of $\mathbf{x}$ and $\mathbf{x}'$, are not in the same vortex, (4) can be approximated by $\mathcal{E}_{kin}\propto\rho q_{ext,kin}^2 a^4$. The conservation of $\mathcal{E}_{kin}$ and $q_{ext,kin}$ then implies that ρa^4 is constant. Numerical experiments of [1] show algebraic growth or decay of various vortex properties. By assuming $a\propto t^{\xi/4}$, we thus have $\rho\propto t^{-\xi}$ or vice versa. Thus, only the one scaling exponent ξ needs to be determined numerically in order to obtain a complete picture of the evolution of vortex properties.

In complete analogy, the opposite special case $a \gg L_D$ leads to $\mathcal{E}_{pot}\propto\rho q_{ext,pot}^2 a^2 L_D^2$ [2]. By assuming $a\propto t^{\chi/2}$, we thus have $\rho\propto t^{-\chi}$ or vise versa, leaving χ the only scaling exponent to be determined numerically.

For the general case, for which a ranges from $a \ll L_D$ to $a \gg L_D$, we use in the following in principle the same approach. First, we express the constant energy density, now $\mathcal{E}$, as a product that contains the vortex density ρ, the constant potential vorticity extremum, now q_{ext}, and the average vortex radius a. The expression for $\mathcal{E}$, derived below, is given by (10b). Using this expression and assuming the algebraic growth of a in (11a), which is verified by numerical experiments in the next section and shown in Fig. 3(b), we thus obtain the algebraic decay law for ρ in (11b), leaving finally ξ the only scaling exponent to be determined numercially.

To implement this approach, we begin by considering

$$\mathcal{E}_{kin}=\frac{1}{2}\rho q_{ext,kin}^2\alpha_{kin}^2 a^4 \qquad (5a)$$

and

$$\mathcal{E}_{pot}=\frac{1}{2}\rho q_{ext,pot}^2\alpha_{pot} a^2 L_D^2. \qquad (5b)$$

The derivations of both expressions are the same as those for the two special cases described above, only that here we retain the factor $1/2$ and introduce the constant parameters α_{kin} and α_{pot} since we are in this general case required to consider the actual identities in (5) rather than merely the proportionalities. To be more specific, note that q_{kin} in (4) is approximated by $q_{ext,kin}$, thus leading to (5a). To compensate for this approximation so that the identity in (5a) is guaranteed, the actual area $a^2\pi$ covered by an average vortex must therefore be reduced to an effective area $\alpha_{kin}a^2$, where π is incorporated in α_{kin}. The parameter α_{pot} is used to fulfill the same purpose in the case of $\mathcal{E}_{pot}$.

Note that in the present general case $q_{ext,kin}$ and $q_{ext,pot}$ are not constant and therefore must be expressed in terms of the constant q_{ext}, which is achieved in the following, resulting in (9). Equation (5) gives

$$\frac{\mathcal{E}_{pot}}{\mathcal{E}_{kin}}=\frac{q_{ext,pot}^2}{q_{ext,kin}^2\sigma\hat{a}^2}, \qquad (6)$$

where $\sigma=\alpha_{kin}^2/\alpha_{pot}$ and $\hat{a}=a/L_D$. An alternative expression of the same fraction is obtained by using again (2) but without manipulating $\mathcal{E}_{kin}$ in terms of the Green function that leads to (4). Introducing ψ/a_ψ as a scale for $\nabla\psi$ and $\hat{a}_\psi=a_\psi/L_D$, the alternative to (6) thus is

$$\frac{\mathcal{E}_{pot}}{\mathcal{E}_{kin}} = \frac{\int_{L^2} (L_D^{-1}\psi)^2 dx}{\int_{L^2} (\nabla\psi)^2 dx} = \hat{a}_\psi^2. \tag{7}$$

Note that with the introduction of a_ψ, we now have two different average vortex radii. The difference is that a and a_ψ are the average vortex radii of the vortices as they appear in the potential vorticity field q and the streamfunction field ψ, respectively.

Combining both fractions (6) and (7) gives

$$\frac{q_{ext,pot}^2}{q_{ext,kin}^2 \sigma \hat{a}^2} = \hat{a}_\psi^2. \tag{8}$$

This is a condition that the desired expressions for $q_{ext,kin}$ and $q_{ext,pot}$ must satisfy while also having the limits implied by (1b), which are

$$q_{ext,kin} \to q_{ext} \text{ and } q_{ext,pot} \to 0 \text{ as } \hat{a} \text{ and } \hat{a}_\psi \to 0,$$

$$q_{ext,kin} \to 0 \text{ and } q_{ext,pot} \to q_{ext} \text{ as } \hat{a} \text{ and } \hat{a}_\psi \to \infty.$$

Suitable expressions are

$$q_{ext,kin}^2 = q_{ext}^2 \frac{1}{1 + \sigma \hat{a}_\psi^2 \hat{a}^2} \tag{9a}$$

and

$$q_{ext,pot}^2 = q_{ext}^2 \frac{\sigma \hat{a}_\psi^2 \hat{a}^2}{1 + \sigma \hat{a}_\psi^2 \hat{a}^2}. \tag{9b}$$

These now allow to express the constant energy density $\mathcal{E}$ as a product containing the vortex density ρ, the constant potential vorticity extremum q_{ext}, and the average vortex radius a, just like for the special cases. Using (5a), (7), and (9a), we have

$$\mathcal{E} = \left(1 + \frac{\mathcal{E}_{pot}}{\mathcal{E}_{kin}}\right)\mathcal{E}_{kin} = (1 + \hat{a}_\psi^2)\frac{1}{2}\rho q_{ext,kin}^2 \alpha_{kin}^2 \hat{a}^4 L_D^4 \tag{10a}$$

$$= (1 + \hat{a}_\psi^2)\frac{1}{2}\rho q_{ext}^2 \frac{1}{1 + \sigma \hat{a}_\psi^2 \hat{a}^2} \alpha_{kin}^2 \hat{a}^4 L_D^4. \tag{10b}$$

The same result is obtained, as it is expected, by expressing $\mathcal{E}$ in (10a) by $(\mathcal{E}_{kin}/\mathcal{E}_{pot}+1)\mathcal{E}_{pot}$ and then using (5b), (7), and (9b).

The remarkable result of our numerical experiments, presented in the next section, is the fact that the algebraic growth of the average vortex radius a is unaffected, especially it is unaffected by the deformation radius L_D [Fig. 3(b)]. For the entire range from $a \ll L_D$ to $a \gg L_D$, we can thus state

$$a = L_D \hat{t}^{\xi/4}, \tag{11a}$$

where time t is normalized as $\hat{t} = t/t_0$ with t_0 being a constant that has to be chosen such that $a = L_D$ at $t = t_0$. Our numerical experiments show that the other average vortex radius a_ψ does not precisely grow algebraically but is nevertheless also a monotonically increasing function of $\hat{t}$. Using (10b) and (11a), the decay of the vortex density ρ is consequently given by

$$\rho = \frac{2\mathcal{E}}{q_{ext}^2 \alpha_{kin}^2 L_D^4} \frac{1 + \sigma \hat{a}_\psi^2 \hat{t}^{\xi/2}}{1 + \hat{a}_\psi^2} \hat{t}^{-\xi}, \tag{11b}$$

which has the two limits

$$\rho = \frac{2\mathcal{E}}{q_{ext}^2 \alpha_{kin}^2 L_D^4} \hat{t}^{-\xi} \text{ as } \hat{t} \to 0 \tag{11c}$$

and

$$\rho = \frac{2\mathcal{E}}{q_{ext}^2 \alpha_{pot} L_D^4} \hat{t}^{-\xi/2} \text{ as } \hat{t} \to \infty. \tag{11d}$$

Note that neither limit depends on $\hat{a}_\psi$ and thus they are identical to the previously studied two special cases $a \ll L_D \to \infty$ [1] and $a \gg L_D$ [2], respectively, but only if $\chi = \xi/2$. This required identity is addressed in the following two sections. The analogy of this scaling theory of the general case to those of the special cases would be complete if we could replace $\hat{a}_\psi$ by $\hat{a}$. This is generally not possible because $\hat{a}_\psi$ and $\hat{a}$ are, as mentioned above, differently defined length scales, which also grow differently. However, the numerical experiments in the next section show that replacing $\hat{a}_\psi$ by $\hat{a}$ causes no visible difference in the result given by (11b). On this basis we can claim complete analogy.

In the next section, we use numerical experiments to verify the assumptions, test the theoretical predictions, and determine the unknown parameters of the scaling theory.

III. NUMERICAL EXPERIMENTS

A. Model

We numerically simulate the free evolution of a random initial state as described by (1). Because the energy cascades only predominantly to larger length scales, there is also some energy that cascades to smaller length scales. For instance, the merger of two vortices can produce filaments that become increasingly thinner. In the physical, continuous case, the energy would thus cascade to increasingly smaller length scales until it would be converted into heat by molecular diffusion. In the discrete case of our numerical model, we have a finite smallest length scale and therefore the spreading of energy to length scales smaller than that smallest length scale must be mimicked by adding a so-called hyperviscosity of the form $-\nu\nabla^2\nabla^2 q$, to the right-hand side of (1a). We set $\nu = 3.5 \times 10^{-9}$, which is chosen sufficiently small thus causing the energy to decrease so little that it can still be considered to be constant. The conservation of potential vorticity extremum q_{ext} is least affected by hyperviscosity because the individual extrema are at the core of the vortices whose size represents the largest length scale in the model and thus they are comparatively insulated from hyperviscosity [13]. However, hyperviscosity becomes an issue when we compare our work with previous work in Sec. IV. The Arakawa scheme [14] is chosen to numerically determine the Jacobian $J(\psi, q)$ in (1a) because it has the important property of conserving

energy and enstrophy, which is crucial since the conservation of energy and enstrophy form the base of geostrophic turbulence and in particular the scaling theory to be tested. The integration in time is done by the Adams-Bashforth scheme and (1b) is Fourier-transformed in order to invert the potential vorticity q to obtain ψ. The boundary condition in space is periodicity in both directions. For the size of the square domain we choose length $L=\pi$. Using a 256×256 grid, gives a grid spacing of $ds=0.012$. For the time step we choose $dt=0.0025$, which we change during the numerical experiment to fulfill the CFL criterion. The random initial state, as specified in the Introduction, has an energy spectrum that has the shape

$$E(|\mathbf{k}|) \propto \frac{|\mathbf{k}|^6}{(|\mathbf{k}|+2|\mathbf{k}_0|)^{18}} \tag{12}$$

and a size such that the energy density in (3a) becomes $\mathcal{E}=0.5$. The maximum of the energy spectrum is at $|\mathbf{k}_0|=30$. Our model is thus almost identical to that used in previous work [9] (see also [15]). The only difference to [9], which is worth mentioning, is his larger domain size $L=2\pi$ and therefore the necessary larger 450×450 grid.

The McWilliams vortex census [9] is employed to determine the average vortex radius a and the vortex density ρ. Its principle mechanism is briefly described in the Introduction. To ensure best possible results, we always visually examine whether the McWilliams vortex census is identifying all coherent vortices at all times.

B. Quadruplication

As geostrophic turbulence freely evolves in our numerical model the vortices grow larger and become fewer until the statistical end state of a single pair of opposite-signed vortices is reached [16]. It is possible that this end state is reached before the average vortex radius a has grown from $a\ll L_D$ to $a\gg L_D$. This could be avoided by having initially a larger number of vortices, which is achieved by enlarging the domain. Because we would have to keep the same resolution, enlarging the domain is computationally expensive. A computationally less expensive method is to enlarge the domain only at a later time when the vortices have become too few. At that time, they have also become larger and therefore the resolution can be reduced, thereby still resolving the vortices sufficiently. This procedure can be repeated several times throughout the evolution.

In order to enlarge the domain we take advantage of the periodic boundary condition in both directions. This particular boundary condition allows us to imagine an infinite plane that is made up of an infinite number of identical copies of the free evolution of geostrophic turbulence in our original domain. Although this allows to consider for instance a larger domain consisting of four copies [Fig. 2(a)], the geostrophic turbulence would not evolve truly in this quadrupled domain. The statistical end state would be an identical pair of opposite-signed vortices in each quadrant. The double periodicity within the four quadrants must therefore be broken at the time when the domain is quadrupled. This is best achieved by having a slightly different state of geostrophic turbulence in each quadrant, which can be obtained by taking the state of the geostrophic turbulence in the original domain at four close consecutive points in time during the evolution and patching them up to obtain the quadrupled domain. These four states should not have any vortices on their boundaries to avoid discontinuities in the resulting quadrupled domain on the boundaries where the four states are connected. If they do, we use the fact that the state of the geostrophic turbulence contained within the dashed box in Fig. 2(a) is identical to the state in the original domain regardless where the box is positioned. The position shown in Fig. 2(a) defines a suitable alternative original domain that turns out to have no vortices on its boundary at the time shown in the figure and at further three close consecutive points in time. Patching up those four states and then halving the resolution gives Fig. 2(b). This quadruplication could be

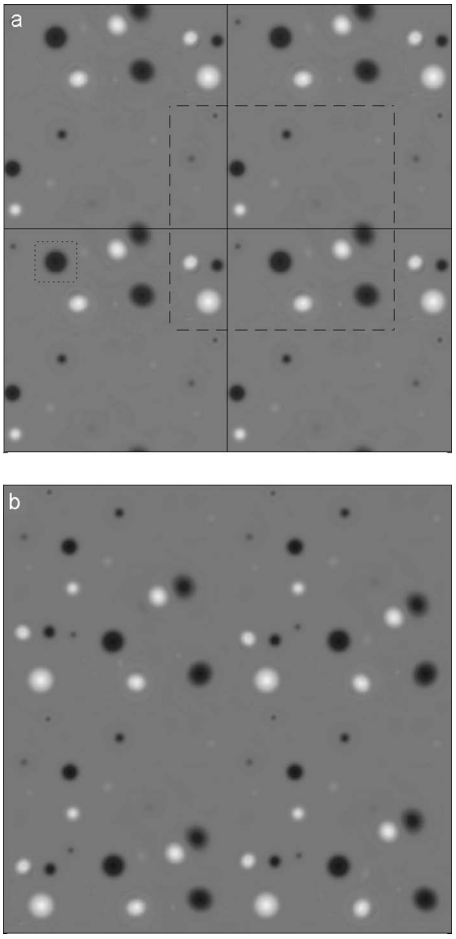

FIG. 2. Quadruplication. Both panels show geostrophic turbulence in the potential vorticity field q, where white indicates $q>0$ and black $q<0$. In (a), the state of geostrophic turbulence in each quadrant and in the dashed box is identical because of the double periodic boundary condition of the original domain that is represented by one quadrant. The dashed box defines an alternative original domain with the advantage of having no vortices on its boundary during a brief period of the evolution of the geostrophic turbulence. During this period, we obtain at four close consecutive times four slightly different states. These four states are patched up and the resolution is halved, which gives (b). The dotted box in (a) defines the section shown in Fig. 1.

automated but because of the few times it must be carried out we have selected the position of the dashed box, that defines the alternative original domain, by visual inspection. It is remarkable how little the patched up states in Fig. 2(b) have to differ from each other to break the double periodicity. The successful breaking is confirmed by the fact that the statistical end state of the geostrophic turbulence shown in Fig. 2(b) is a single pair of opposite-signed vortices, as opposed to that of Fig. 2(a), which is four pairs.

We can only halve the resolution, and therefore quadruple the domain, when the average vortex radius a has doubled since the start of the evolution or since the last quadruplication. Assuming a doubles between times t and ct, the constant c must therefore, according to (11a), satisfy $(ct)^{\xi/4}=2t^{\xi/4}$, which gives $c=2^{4/\xi}$.

If the evolution is in the phase for which $a \ll L_D$, the number of vortices (vortex density ρ), evolving according to (11c), decreases between the above times by a factor of $(t)^{-\xi}/(ct)^{-\xi}=16$. This implies that the quadruplication scheme is limited because it cannot produce a sufficient number of vortices indefinitely. For example, if we started with 512 vortices, only 32 would exist by the time a would have doubled. Quadrupling the domain at this time would increase the number of vortices to 128 and not back to 512. Alternatively, if we quadrupled the domain whenever the number of vortices has decreased by a factor of 4, a would not yet have doubled but only increased by a factor of $\sqrt{2}$. Halving the resolution in this case would render it to be too low to resolve the vortices. This alternative scheme has in principle been implemented in a study of a point-vortex model in the case $a \ll L_D \to \infty$ (two-dimensional turbulence) [15], in which it is called renormalization. In this study, the domain is, after being quadrupled, shrank to its original size. This reduces a by a factor of 2. However, consistency with scaling theory, given in this case by (11a) and (11c), would dictate a factor of $\sqrt{2}$, which can be understood by imagining the evolution to reverse in time. In this reversal, increasing the number of vortices by a factor of 4 would reduce a not by a factor of 2 but of $\sqrt{2}$. Because the renormalization scheme, nevertheless, reduces a by a factor of 2 and not of $\sqrt{2}$, it does not continue the same evolution of two-dimensional turbulence but defines a new and different state of two-dimensional turbulence every time it is implemented. This is not the case for our quadruplication scheme, which is consistent with scaling theory, but it is still limited due to the same reason the renormalization scheme is limited.

If the evolution is in the phase for which $a \gg L_D$, the number of vortices (vortex density ρ), evolving according to (11d), decreases not by a factor of 16, as in the case above, but only of 4. Thus, in this case the quadruplication scheme can be applied indefinitely many times, allowing the evolution to be numerically simulated for an arbitrary long time thereby always having a sufficient number of vortices.

C. Results

The results of the numerical experiments are presented in Fig. 3. In this section, after a comment about quadruplication, we first show that the numerical experiments verify the assumptions that form the base of the scaling theory in Sec. II, then collect the values of the parameters that the scaling theory cannot provide, and finally summarize the results.

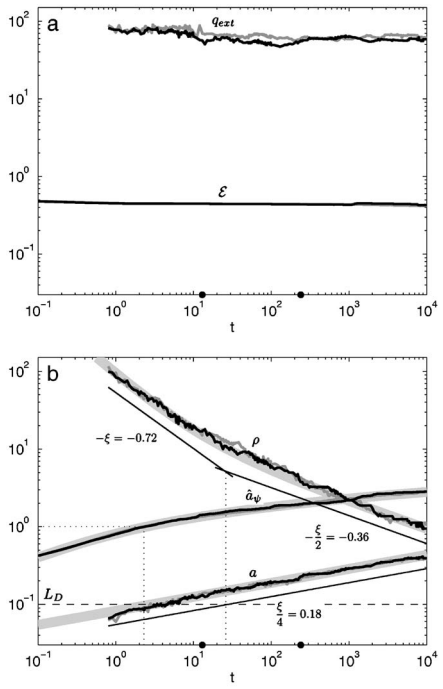

FIG. 3. Results. The thin black graphs are produced by the numerical experiment described in Sec. III. The times of quadruplication are indicated by the two large dots on the t axis. The thin dark grey graphs are produced by a numerical experiment that is identical except that it uses a 16 times larger domain on a 1024×1024 grid and therefore no quadruplications. During the free evolution of an initial random state, most identifiable coherent vortices begin to emerge only after some time has elapsed, here at $t \approx 0.8$. Therefore, the potential vorticity extremum q_{ext}, the average vortex radius a and the vortex density ρ are not determined until then. The thick light grey graphs represent the assumption for a in (11a), the prediction for ρ in (11b), and the best fit for $\hat{a}_\psi$, given by $\hat{a}_\psi = \log\sqrt{40\hat{t}}+2.4$.

In our main numerical experiment, as described in the previous two subsections, we quadruple the domain twice during the evolution. This is compared with a numerical experiment that is identical except that it uses a 16 times larger domain on a 1024×1024 grid and therefore no quadruplications. Figure 3 (thin black graphs with quadruplication; thin dark grey graphs without quadruplication) shows that the quadruplication has no noticeable effect, as desired.

The scaling theory is based on the assumption that the energy density $\mathcal{E}$, the potential vorticity extrema q_{ext}, and the exponent $\xi/4$ of the algebraic growth of the average vortex radius a in (11a) remain constant throughout the entire evolution. Figure 3 clearly shows that the numerical experiments verify all these assumptions.

It is remarkable that the growth of the average vortex radius a, seen in Fig. 3(b), is unaffected, especially it is unaffected by the deformation radius L_D, as opposed to the vortex density ρ. As mentioned in the Introduction, we are free to shift a in Fig. 3(b) such that $a=L_D$ at the same time t

at which the slope of ρ changes (see also last paragraph of this section). The unprecedented long and unaffected growth over a period of about four decades allows determining $\xi = 0.72$ in (11a) with good accuracy.

Regarding the vortex density ρ, we first consider the special cases $a \ll L_D$ [$t \to 0$ in Fig. 3(b)] and $a \gg L_D$ [$t \to \infty$ in Fig. 3(b)]. For these two limits, Fig. 3(b) indicates an algebraic decay of ρ with an exponent of -0.72 and -0.36, respectively. This is consistent with our scaling theory, which predicts the former exponent to be twice the latter [Eqs. (11c) and (11d)]. Additional consistency is given by the fact that the algebraic decay of ρ gives $\xi = 0.72$, which is the same as that given by the algebraic growth of a. It is important to point out that the exponents in terms of which ρ and a are expressed, are determined by two independent methods employed by the McWilliams vortex census, as described in the Introduction. In simple terms, counting vortices is clearly unrelated to determining their average radius. Both of these independent methods lead to $\xi = 0.72$, thus showing this additional agreement between our scaling theory and numerical experiments.

In order to determine the two remaining parameters α_{kin} and α_{pot}, we collect various parameter values from Fig. 3. One is $t_0 = 2.3$ in (11a). Others are $q_{ext} = 60$ and $\mathcal{E} = 0.44$, rather than $\mathcal{E} = 0.5$, as specified in Sec. III A. We use a smaller value of $\mathcal{E}$ because $\mathcal{E}$ decreases in a very short initial period up to about $t = 0.2$ from 0.5 to 0.47. During this period some energy is still in such small length scales that it is effectively dissipated by the hyperviscosity. However, for the remaining evolution $\mathcal{E}$ decays very slowly and can be taken to be $\mathcal{E} = 0.44$. We can now set the values of α_{kin} and α_{pot} such that the values of the limits of ρ in the scaling theory (11c) and (11d) agree with those of the numerical experiments in Fig. 3(b). This gives $\alpha_{kin} = 0.44$ and $\alpha_{pot} = 0.35$. The effective areas, mentioned below (5), thus become $0.06a^2\pi$ and $0.04a^2\pi$, respectively.

The case that remains to be considered is $a \approx L_D$, which requires $\hat{a}_\psi$. Figure 3(b) shows that $\log\sqrt{40\hat{t}} + 2.4$ fits $\hat{a}_\psi$. Because this fit is only required to be valid for $a \approx L_D$, it does not matter that $\hat{a}_\psi$ does not tend to zero as $\hat{t} \to 0$, as it should if it had to be valid for the entire range of a.

The average vortex radius a and the vortex density ρ, as given by the scaling theory (11a) and (11b), respectively, are now fully determined and shown by Fig. 3(b) (thick light grey graphs) to be in good agreement with our numerical experiments.

In Sec. II. it is pointed out that a complete analogy to the special cases is spoiled by the introduction of the second average vortex radius a_ψ. However, replacing $\hat{a}_\psi$ in (11b) by $\hat{a}$ gives an expression of ρ that cannot be visually distinguished from the ρ shown in Fig. 3(b) (thick light grey graph). On this basis we can therefore set $\hat{a}_\psi = \hat{a}$ and thus a complete analogy between the scaling theories of the special cases and the general case is established.

It is worth mentioning that the definition of the average vortex radius a is not fixed. As described in the Introduction, the McWilliams vortex census determines a by choosing the vortex boundary to be where $q = 0.2q_{ext}$. This choice turns out to give $a = L_D$ when $\hat{a}_\psi = 1$ [dotted lines in Fig. 3(b)], that is, when the ratio $\mathcal{E}_{pot}/\mathcal{E}_{kin} = 1$ (7). We could choose a different definition for the radius, say $a_{new} = 0.64a$. This choice might in the current context be more suitable because $a = L_D$ when the transition from $\rho \propto \hat{t}^{-\xi}$ to $\rho \propto \hat{t}^{-\xi/2}$ occurs [dotted line in Fig. 3(b)]. If the definition of a was changed, the resulting change in ρ would be compensated by changing α_{kin} and α_{pot}.

IV. COMPARISON WITH PREVIOUS WORK

By comparing our general case with the two special cases studied previously, we demonstrate agreement after resolving an inconsistency with one of the two special cases.

For the special case $a \ll L_D \to \infty$, [1] show that $a \propto t^{\xi/4}$ and $\rho \propto t^{-\xi}$, with $\xi = 0.75$, which is later corrected to $\xi = 0.72$ [15]. The limit $\hat{t} \to 0$ of our scaling theory [Eqs. (11a) and (11c)] represents this special case and indicates the same algebraic growth and decay, respectively. Our numerical experiments give $\xi = 0.72$. Thus our work fully agrees with [1].

For the special case $a \gg L_D$, [2] show that $a \propto t^{\chi/2}$ and $\rho \propto t^{-\chi}$, with $\chi = 0.55$ determined numerically. The limit $\hat{t} \to \infty$ of our scaling theory [Eqs. (11a) and (11d)] represents this special case and indicates the same algebraic growth and decay, respectively. However, our numerical experiments give $\chi = \xi/2 = 0.36$ [Fig. 3(b)] and not $\chi = 0.55$.

To resolve this inconsistency we review the method by which [2] determine the value of χ. They consider a quantity called U_1, which is given by

$$U_1 = \frac{1}{L^2}\int_{S_{coh}} \frac{1}{2} q \nabla^2 \phi \, d\mathbf{r} \approx -\frac{1}{L^2}\int_{S_{coh}} \frac{1}{2}\lambda^2 \phi \, \nabla^2 \phi d\mathbf{r} \quad (13)$$

[their (14) and (18)], where, in terms of our notation, $\lambda = L/L_D$, $\phi = \psi$, and $\mathbf{r} = \mathbf{x}$. The area of integration S_{coh} is the area that the coherent vortices occupy. It is defined to be where the Gaussian curvature $[\partial^2\phi/(\partial x \partial y)]^2 - (\partial^2\phi/\partial x^2)(\partial^2\phi/\partial y^2)$ is negative and the absolute value of the potential vorticity $|q|$ is larger than the average of $|q|$ taken over the entire domain. They state that (13) leads to $U_1 \propto N\lambda^{-2}q_a^2$ [their (18)], where N is the total number of vortices in the domain and $q_a = \lambda^2\phi$. As they provide no derivation, we suppose that they use S_{coh} and N to define an average vortex radius a_{coh} and take $\nabla^2\phi$ to be scaled as ϕ/a_s^2. From (13), we have $U_1 \propto N\lambda^{-2}q_a^2 a_{coh}^2/a_s^2$. Assuming that a_{coh}^2/a_s^2 is constant during the evolution, gives their result. Since $q_a = \lambda^2\phi \gg \nabla^2\phi$, q_a can be considered constant, resulting in $U_1 \propto N$. Using $N = L^2\rho \propto t^{-\chi}$, the evolution of U_1 therefore determines χ. However, the assumption that a_{coh}^2/a_s^2 is constant during the evolution cannot be generally made. From our numerical experiments we know that two differently defined average vortex radii, in our case a and a_ψ, grow also differently [Fig. 3(b)], and their ratio is therefore not constant during the entire evolution. Consequently, we do not necessarily have $U_1 \propto N$.

We recreate their numerical experiment and instead of determining the decay of U_1, we employ the McWilliams vortex census to determine the decay of the vortex density ρ, to obtain χ. Two crucial differences to our numerical experiments described in Sec. III are worth noting. First, their hy-

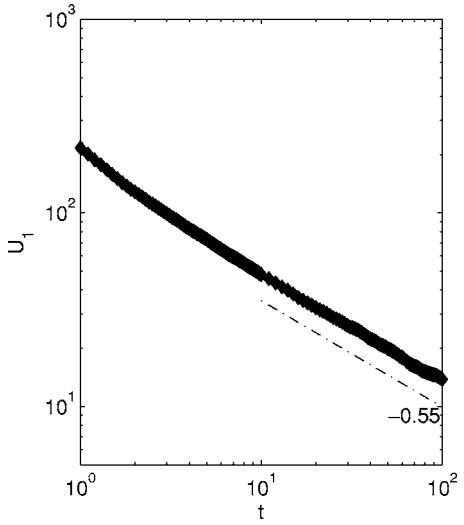

FIG. 4. U_1 in (13). This is the evolution of U_1 produced by the recreation of the numerical experiment of [2]. The slope of −0.55 agrees with the original numerical experiment. Compare with Fig. 8 in [2].

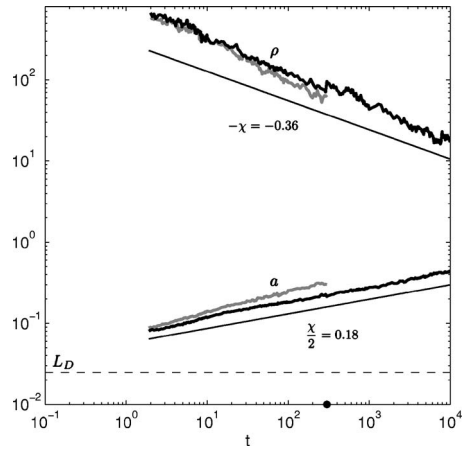

FIG. 5. Recreation of the numerical experiment of [2]. The grey graphs are produced by the recreation of the numerical experiment of [2]. The black graphs are produced by the same numerical experiment, except that the smaller hyperviscosity of Sec. III. is used. For the reason that the average vortex radius a and the vortex density ρ are only shown for later times, refer to the caption on Fig. 3. The quadruplication is marked by the large dot at $t=300$ on the t axis.

perviscosity is much larger than ours in Sec. III. The effect of the two different hyperviscosities is seen in the energy decay. At $t=100$, the energy has decayed in their case by 40% (their Fig. 7), whereas with our smaller hyperviscosity of Sec. III, it has only decayed by 17% (not shown). Second, their maximum of the initial energy spectrum is at $|\mathbf{k}_0|=50$, compared to ours at $|\mathbf{k}_0|=30$ in Sec. III, but both have a 256×256 grid.

Our recreation of their numerical experiment produces the same evolution of U_1 (Fig. 4), featuring the expected slope of −0.55 (compare with their Fig. 8). The evolution of the average vortex radius a has a slope larger than our value of 0.18 (grey graph in Fig. 5). This faster growth might be due to the large hyperviscosity, which diffuses the vortices, thus making them larger than they would be with a smaller hyperviscosity. To test this hypothesis, we reduce the hyperviscosity to our value in Sec. III. In this case, the evolution of a has a slope of 0.18 (black graph in Fig. 5). Returning to their larger hyperviscosity, the slope of the evolution of ρ (grey graph in Fig. 5) is slightly larger than our value of −0.36. This might be due to more frequent mergers of vortices possibly because of their enlarged size caused by the larger hyperviscosity. Reducing again the hyperviscosity as above, the slope of the evolution of ρ (black graph in Fig. 5) is closer to the value of −0.36. We can conclude that by reducing the hyperviscosity to our value given in Sec. III, so that the important property of conservation of energy and enstrophy is approximately guaranteed, the recreation of their numerical experiment with our hyperviscosity produces results that are in complete agreement with our scaling theory and numerical experiments.

It is worth noting that the recreation of their numerical experiment with our hyperviscosity is always close to becoming unstable, especially during the early part of the evolution. Therefore, the results are not as clear as they could be. The reason is that by setting $|\mathbf{k}_0|=50$, too much energy is contained in small scales partly spreading towards the smallest resolved length scale. Our small hyperviscosity is unable to remove this energy effectively. Its presence disturbs the emergence of coherent vortices and they appear fringed. For this reason, we choose for our numerical experiments in Sec. III $|\mathbf{k}_0|=30$. It is not an alternative to keep $|\mathbf{k}_0|=50$ and to increase instead the hyperviscosity as is done in their experiments because the geostrophic turbulence must be virtually inviscid, that is, conserve energy, in order to test the scaling theories.

V. SUMMARY

As geostrophic turbulence governed by (1) evolves freely from a random initial state coherent vortices emerge. By merging, they grow and become fewer. The average vortex radius a and the number of vortices in the domain or vortex density ρ are determined by the McWilliams vortex census. It is remarkable, as shown by our numerical experiments (Fig. 3), that the growth of a from $a\ll L_D$ to $a\gg L_D$ remains unchanged and in particular is not affected by the deformation radius L_D. We find that $a\propto\hat{t}^{\xi/4}$ with $\xi=0.72$. This expression for a forms the base of the derivation of our scaling theory, which concludes with an expression for ρ, given by (11b). It predicts the decay of ρ as seen in our numerical experiments, which thus verify our scaling theory and in particular also the value $\xi=0.72$ independently determined by the growth of a. In the limit $a\ll L_D$, $\rho\propto\hat{t}^{-\xi}$, and thus our work agrees with that of [1], who consider the case $a\ll L_D\to\infty$. In the limit $a\gg L_D$, $\rho\propto\hat{t}^{-\xi/2}$ which does not agree with the work of [2], who consider the same case but obtain a larger value for $\xi/2$ (their χ). This inconsistency is resolved by first pointing out that their hyperviscosity is too large and then recreating their numerical experiment with our smaller hyperviscosity.

In summary, as the average vortex radius a grows unaffected, especially it is unaffected by the deformation radius L_D, as $a \propto \hat{t}^{\xi/4}$ through a large range from $a \ll L_D$ to $a \gg L_D$, the decay of the vortex density ρ is slowed down from $\rho \propto \hat{t}^{-\xi}$ to $\rho \propto \hat{t}^{-\xi/2}$ when a has grown to be comparable to L_D.

VI. APPLICATION

The result of this paper has already been used in the study of an energy cascade toward the equator, which might be relevant to physical oceanography [11]. For the components of the ocean dynamics that depend on depth, so-called baroclinic modes, the corresponding deformation radii depend on latitude. We therefore consider in this section a latitude-dependent deformation radius. As specified in the Introduction and throughout this paper, except in this section, we consider an f plane, given by a constant Coriolis parameter $f=f_0$, and thus the deformation radius $L_D=\sqrt{g'H}/f_0$ is also constant. To introduce the latitude-dependence of $f=2\Omega \sin\theta$ (see Introduction), a β plane, given by the approximation $f=f_0+\beta y$, where β is a constant and y the meridional direction, is usually considered. Despite of this, the derivation of the well-studied form of the QG equation on a β plane (e.g., [6] Sec. 12.2, [7] Sec. 3.12, [5] Sec. 2.6), gives the same constant deformation radius $L_D=\sqrt{g'H}/f_0$ as in the case of an f plane. We therefore make the unconventional step of allowing L_D nevertheless to be latitude-dependent by replacing f_0 by $f=f_0+\beta y$ [17]. A formal derivation that justifies this unconventional step is given by [11], Appendix A. It is worth noting that the β-plane approximation adds the term βy to the right-hand side of (1b), which gives rise to Rossby waves. To simplify our study we omit this term, which removes the Rossby waves from the dynamics, and thus represents the high energy limit. A full analysis and discussion of this omission is given in [11].

The above changes leave all equations in this paper formally unchanged, particularly the energy density $\mathcal{E}$ and enstrophy density $\mathcal{Z}$ in (3), which remain formally unchanged even if we do not omit the term βy. Following the same argument as below (3), we find that in this case energy cascades not only to larger length scales but also to larger L_D, that is, toward the equator [17].

We know that the energy cascade to larger length scales manifests itself in merging vortices. It is of interest to know how the equatorward energy cascade manifests itself. The result of this paper suggests part of a manifestation. Since the deformation radius is now latitude-dependent, we have to consider a latitude-dependent average vortex radius a and vortex density ρ. Suppose we consider vortices for which a is initially smaller than the smallest L_D of the model. Throughout the free evolution of the geostrophic turbulence the vortices grow according to $a \propto \hat{t}^{\xi/4}$, unaffected by L_D and thus independent of latitude. The decay of ρ in this evolution is slowed down from $\rho \propto \hat{t}^{-\xi}$ to $\rho \propto \hat{t}^{-\xi/2}$ first where L_D is smallest, that is, at the highest latitudes. As a continues to grow, the decay of ρ is slowed down at consecutively lower latitudes. This creates a field of same-sized vortices whose density ρ decreases with latitude. Figure 6 shows such a field with many vortices at high latitudes (top and bottom of figure) and few around the equator (middle of figure). Vortices then begin to move to where there is more space (low ρ), which is at lower latitudes. Since the vortices contain most of the energy of the geostrophic turbulence, the energy thus moves or cascades to lower latitudes, that is, toward the equator. An equatorward energy cascade might occur in the ocean because energy is observed to increase toward the equator [10].

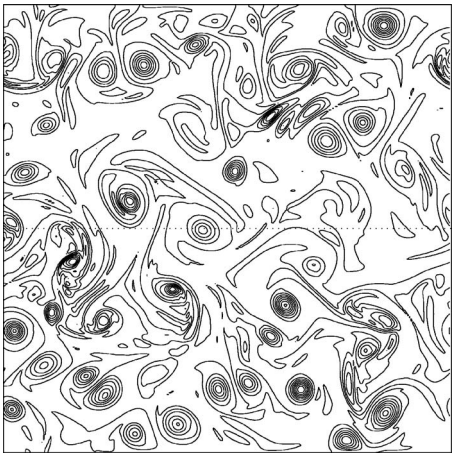

FIG. 6. Latitude-dependent deformation radius. This is the potential vorticity field q of the model described in Sec. VI. The deformation radius increases toward the equator, which is denoted by the dotted horizontal line in the middle. The vortices have approximately the same radius throughout the domain, that is, the value of the average vortex radius is the same at each latitude, but the vortex density decreases towards the equator (figure from [11]).

ACKNOWLEDGMENTS

The author is deeply indebted to his postdoctoral advisor Rick Salmon who generously shared his knowledge of geostrophic turbulence with him. The author is also grateful to George Carnevale and Bill Young, for good suggestions and especially to Colm-Cille Caulfield, who in addition gave advice on the revised manuscript. Detlef Stammer and Bruce Cornuelle are thanked for their support. This work was supported by the National Science Foundation (OCE-0100868).

[1] G. F. Carnevale, J. C. McWilliams, Y. Pomeau, J. B. Weiss, and W. R. Young, Phys. Rev. Lett. **66**, 2735 (1991).
[2] T. Watanabe, T. Iwayama, and H. Fujisaka, Phys. Rev. E **57**, 1636 (1998).
[3] J. Charney, Geophys. Norv. **17**, 1 (1948).
[4] A. Hasegawa and K. Mima, Phys. Fluids **21**, 87 (1978).
[5] R. Salmon, *Lectures on Geophysical Fluid Dynamics* (Oxford University Press, New York, 1998).
[6] A. Gill, *Atmosphere-Ocean Dynamics* (Academic Press, New York, 1982).
[7] J. Pedlosky, *Geophysical Fluid Dynamics*, 2nd ed. (Springer-Verlag, New York, 1987).
[8] G. Carnevale, in *Proceedings of the International Turbulence Workshop, 2003*, University of Central Florida, Orlando, Florida, edited by S. Shivamoggi (Marcel Dekker, New York, 2004).
[9] J. McWilliams, J. Fluid Mech. **219**, 361 (1990).
[10] D. Stammer, J. Phys. Oceanogr. **27**, 1743 (1997).
[11] J. Theiss, J. Phys. Oceanogr. **34**, 1663 (2004).
[12] M. Melander, N. Zabusky, and J. McWilliams, Phys. Fluids **30**, 2610 (1987).
[13] V. Larichev and J. McWilliams, Phys. Fluids A **3**, 938 (1991).
[14] A. Arakawa, J. Comput. Phys. **1**, 119 (1966).
[15] B. Weiss and J. McWilliams, Phys. Fluids A **5**, 608 (1993).
[16] G. Carnevale, J. McWilliams, Y. Pomeau, J. Weiss, and W. Young, Phys. Fluids A **4**, 1314 (1992).
[17] R. Salmon, in *Topics in Ocean Physics*, edited by A. Osborne and P. Rizzoli, Proceedings of the International School Enrico Fermi (North-Holland, Amsterdam, 1982), p. 550pp.